J Solid State Electrochem (2012) 16:2503–2513
DOI 10.1007/s10008-012-1666-y

ORIGINAL PAPER

Kinetics of passivity of NiTi in an acidic solution and the spectroscopic characterization of passive films

Mirjana Metikoš-Huković · Jozefina Katić · Ingrid Milošev

Received: 15 July 2011 / Revised: 22 January 2012 / Accepted: 25 January 2012 / Published online: 15 February 2012

Abstract Anodic polarization of nitinol in acetic acid under galvanostatic conditions produces oxide films composed mainly of TiO_2. An exponential current-field relation is valid during ionic conduction through the growing oxide, in which the field coefficient is related to the jump distance. Transport processes in anodic films have been discussed in terms of a cooperative mechanism developed for amorphous oxide films on valve metals, in which both metal and oxygen ions were involved in ionic conduction. For more crystalline oxide structure of passive films on nitinol, formed during a prolonged potentiostatic conditions, the charge transfer takes place only through the oxygen vacancies as mobile species via a high-field-assisted mechanism. Based on the results of the Mott–Schottky analysis, these films behave as *n*-type semiconductors indicating that oxygen vacancies formed during the film formation and growth act as electron donors. The barrier/protecting and electronic/semiconducting properties of the passive films as well as their chemical composition were studied using electrochemical impedance spectroscopy and X-ray photoelectron spectroscopy.

Keywords Cooperative mechanism of ionic conductivity · Diffusivity of anion vacancies · Titanium · Nickel · Oxide films · Passivity · X-ray photoelectron spectroscopy (XPS) · Electrochemical impedance spectroscopy (EIS)

M. Metikoš-Huković (✉) · J. Katić
Department of Electrochemistry, Faculty of Chemical Engineering and Technology, University of Zagreb,
Savska c. 16, P.O. Box 177, 10000 Zagreb, Croatia
e-mail: mmetik@fkit.hr

I. Milošev
Department of Physical and Organic Chemistry,
Jožef Stefan Institute,
Jamova c. 39,
1000 Ljubljana, Slovenia

List of symbols

a^*	Half-barrier width (jump distance) of energy barrier (nm)
A	Kinetic parameter (A cm^{-2})
B	Field coefficient (cm V^{-1})
C	Capacitance (F cm^{-2})
CPE	Constant-phase element
C_{dl}	Double layer capacitance (F cm^{-2})
C_{sc}	"Space charge" capacitance (F cm^{-2})
d	Oxide layer thickness (nm)
$D_{Ö}$	Diffusion coefficient of oxygen vacancies (cm^2 s^{-1})
e	Electron charge (1.602×10^{-19} C)
E	Potential (V)
E_b	Binding energy (eV)
E_f	Film formation potential (V)
E_{fb}	Flat band potential (V)
E_{OCP}	Open circuit potential (V)
f	Frequency (Hz)
F	Faraday constant (96,500 C mol^{-1})
H	Mean electric field strength (V cm^{-1})
I	Intensity (a.u.)
j	Current density (A cm^{-2})
j_p	Passive current density (A cm^{-2})
$J_{Ö}$	Steady-state flux of oxygen vacancies (s^{-1} cm^{-2})
$j\omega$	Complex variable for sinusoidal perturbations with $\omega=2\pi f$
k_B	Boltzmann constant (1.38×10^{-23} J K^{-1})
n	CPE power
N_D	Donor density (cm^{-3})
M	Molar mass (g mol^{-1})
r	Specific volume of formed oxide per coulomb (cm^3 C^{-1})

r_0	Outer radius of conductive gap (radium of cluster) (cm)
$\Re$	Universal gas constant (8.314 JK^{-1} mol^{-1})
R_{el}	Ohmic resistance (Ω cm^2)
R_{ox}	Resistance of the oxide layer (Ω cm^2)
R_j	Unitary formation rate of the film formation (F^{-1} cm^2)
S	Electrode surface (cm^2)
Q	Constant of the CPE element (Ω^{-1} cm^{-2} s^n)
T	Temperature (K)
t_M	Metal transport number
t_p	Passivation time (h)
V_O^{2+}	Oxygen vacancies (Kroger–Vink notation)
w_2	Experimental parameter (cm^{-3})
z	Number of electrons interchanged
z_O	The charge number of oxygen ions
Z	Electrode impedance (Ω cm^2)
Z_{im}	Imaginary part of impedance (Ω cm^2)
γ	Constant related to overlap of cluster before and after vacancy jump
χ	Stoichiometric parameter for $MO_{\chi/2}$ passive film
Δ	Scofield photoionization cross section
δ	Charge on the cation ejected from the passive film
ε	Dielectric constant of the surface film
ε_o	Dielectric constant of vacuum (8.85×10^{-14} F cm^{-1})
λ	Inelastic mean free electron path (nm)
ν	Scan rate (mV s^{-1})
σ	Surface roughness factor
ρ	Density (g cm^{-3})
ω	Angular frequency (Hz)

Introduction

Nitinol (NiTi), an implant material, derives the attractiveness from superelasticity and shape memory effect, meaning the crystal structure changes between martensite (low temperature, soft form) and austenite structure (high temperature, rigid form) [1, 2]. Nitinol is emerging as an important and promising material to develop state-of-the-art devices in the medical (stents for the expansion of coronary arteries) and the dental field (orthodontic fasteners and wires) [3]. Another application is a staple for broken bones, which needs to keep its shape during insertion, and then the shape memory effect of nitinol becomes useful for fastening separated bones tightly and to accelerate the healing process.

Titanium and its alloys have been extensively used as implant materials due to its high chemical corrosion resistance in the physiological solutions (body fluids) caused by the passive native oxide film of TiO_2 [1, 4]. Although nitinol is near-equiatomic nickel titanium alloy, the surface natural film (spontaneously formed in air or aqueous solution) consists mainly of TiO_2 because oxidation of Ti is thermodynamically more favorable process than that of Ni [5]. However, in a long-term contact with aggressive body fluids, nitinol corrodes by releasing Ni^{2+} ions that act as an allergen for many people [6]. Corrosion of the nitinol wire in endovascular grafts was confirmed by analyzing samples obtained from patients in Germany and France. The observed pitting and irregularly shaped corrosion defects were the precursors of materials failure [7]. In addition, presence of localized corrosion is usually more difficult to detect than general corrosion. Thus, to prevent the unwanted nickel dissolution, the surface properties of nitinol have been modified using different coatings or other surface treatments [4, 8, 9].

Among these techniques, the thickening of the spontaneously formed natural oxide film on nitinol by anodic polarization in appropriate electrolyte solutions has resulted in improved corrosion resistance, one of the biocompatibility key-governing factors for nitinol implantation [10–13]. Also, the high voltage anodization was carried out in various electrolytes to produce thick porous layers [14]. Anodic oxidation represents an effective way of modifying and controlling the properties of the metal surface [11–13]. It can be expected that thin anodic oxide films have potential for application in areas where the specific surface functionalization by thin films is essential for the quality of the metal implant application.

There is a need for more detailed investigations of nitinol passivation, i.e., kinetics of the oxide film formation and growth as well as characterization of these films (chemical composition, barrier/protecting, and electronic properties). Generally, anodic oxidation of valve metals, e.g., aluminum, tantalum, tungsten, niobium, zirconium, and titanium [15], produces compact, nonporous oxide films which have amorphous structures [16]. During anodic polarization of valve metals, the current density is proportional to the term exp (BH), in which H is the electric field strength in the growing surface film and B is the field coefficient correlated to the jump distance [17, 18].

A number of authors have discussed the ionic conduction in the oxide films using cooperative mechanism of metal and oxygen ions transport, which arises from the amorphous structure (certain lability of the oxide structure is required) [16]. The fraction of current carried by metal ions is denoted by t_M. It was found that the metal ion transport varies from 0.1 to 0.5 in the various systems [18–20] and increases with electric field [20]. Oxygen transport occurs via exchange between transported oxygen ions and those constituting the film. For crystalline oxides, the exchange would result from vacancy or interstitial transport, although such distinction is less meaningful in amorphous materials. Models for conduction in amorphous and crystalline oxide films have evolved over time to include new concepts derived from experimental results [21–23]. Mathematical model was developed by Wang and Hebert [24] for a cooperative ion

conduction mechanism, i.e., for metal and oxygen ion transport in amorphous anodic oxide films on valve metals. Conduction of ionic charge in the oxide films in the model involves jumps of oxygen ions into vacancy together with its associated mobile metal ions (referred to as "defect cluster").

The metal transport number, t_M, is expressed as

$$t_M = \frac{6\pi\gamma H\varepsilon\varepsilon_0 r_0^2}{6\pi\gamma H\varepsilon\varepsilon_0 r_0^2 - z_O e} \quad (1)$$

where H is the electric field strength, z_O is the charge number of oxygen ions, e is the electron charge, ε and ε_0 are dielectric constants of oxide film and vacuum, respectively, γ and r_0 are constants defined by "defect cluster" model [24]. According to Eq. 1, the transport number is independent of cluster concentration but depends on the electric field, permittivity, and cluster radius. It is noteworthy to mention that the practical range of fields for high-field conduction is very small and comparison of t_M in the wide range of fields may not be possible.

On the other hand, the cooperative transport does not occur in crystalline oxides, and transport number of either metal or oxygen is zero, since these conditions imply a rigid lattice or sublattice oxide structure [16, 18]. For crystalline passive oxide films with semiconducting properties, only one type of charge carriers prevails (passive films on Fe, Ni, and Ti). The growth of the oxide films is controlled by the transport rate of point defects (metal and oxygen vacancies) through the film [23, 25]. The key parameter in describing the migration and consequently the kinetics of the oxide film growth is diffusivity of point defects. The band-structure model of the passive film can be employed to explain the oxidation process in terms of lattice ionic defects and the oxide film growth mechanism.

To the best of our knowledge, no results have been reported concerning the kinetics of the oxide film growth on nitinol. Thus, the main goal of this paper is to study the kinetics of the oxide film formation and growth and additionally to characterize passive films formed as well as to characterize the barrier/protecting properties and the chemical composition of the passive oxide film potentiostatically formed on nitinol surface.

Experimental

The nitinol foil (NiTi; Alfa Aesar, 55.82 wt.% Ni, ≤0.05 wt.% C, ≤0.05 wt.% O, ≤0.20 wt.% other metal impurities, and balance Ti) was cut into 0.38-mm-thick disks 13 mm in diameter. The circular-shaped electrodes of nitinol and pure nickel were abraded successively with SiC papers of 240 to 1,200 grit and polished in alumina suspensions (particle size 1, 0.3, and 0.05 μm). They were then cleaned ultrasonically with acetone and redistilled water and degreased in isopropyl alcohol. The PAR Corrosion cell system, model K47, was used. The counter electrode consisted of two graphite rods and the reference electrode, to which all potentials in the paper are referred, was Ag | AgCl in 3.0 mol dm^{-3} KCl (E=0.210 V_{SHE}) [26]. The surface area of the working electrodes was 1 cm^2. Cyclic voltammograms of bare nickel and nitinol were recorded in 1 M acetic acid in the potential range from −1.5 to +1.5 $V_{Ag|AgCl}$ with a scan rate of 10 mV s^{-1}.

Polarization measurements were made on nitinol in 1 M acetic acid using the conventional galvanostatic technique, and the potential-time curves were measured at constant current densities (30–100 μA cm^{-2}). Also, potentiostatic current–time transients were recorded on nitinol by applying a potential pulse from −1.5 $V_{Ag|AgCl}$ to various film formation potentials, ranging from 0.5 to 1.0 $V_{Ag|AgCl}$, at which the electrode was polarized for 24 h. The film formation time for all specimens was 24 h. The samples passivated in this way were used in studying the oxide film properties in 1 M acetic acid by electrochemical impedance spectroscopy (EIS) and Mott–Schottky (MS) method.

EIS measurements were performed in the frequency range from 100 kHz to 5 mHz at an ac voltage amplitude of ±5 mV using a Solartron frequency response analyzer SI 1260 and a Solartron electrochemical interface 1287 controlled by a personal computer. The experimental data were fitted using the complex nonlinear least squares (CNLS) fit analysis software, ZView®, and values of elements of the proposed equivalent circuit were derived with χ^2 values less than 2×10^{-3} (errors in parameter values of 0.5–3%). The space charge capacitance values of the nitinol | solution interface, required for a Mott–Schottky analysis, were determined at a constant frequency of 100 Hz. The imaginary part of the impedance, Z_{im}, was measured as a function of the electrode potential, and the interfacial capacitance, C, was obtained from the relationship $C=-1/\omega Z_{im}$. The potential was swept in the negative direction from the oxide formation potential at a sweep rate (50 mV s^{-1}) sufficiently high for the layer thickness to remain constant.

Surface analysis

X-ray photoelectron spectroscopy (XPS) was performed with a TFA Physical Electronics Inc. spectrometer using non- and monochromatized Al K_α radiation (1,486.6 eV) and a hemispherical analyzer. The monochromatized radiation used for high-resolution spectra yields a resolution of 0.6 eV, as measured on an Ag $3d_{5/2}$ peak. These spectra were used to differentiate between various species, i.e., to study the chemical environment, whereas spectra obtained, using the non-monochromatized variation, were used for

quantifying the chemical composition. The take-off angle used, defined as the angle of emission relative to the surface, was 45°. The energy resolution was 0.5 eV. Survey scan spectra were recorded at a pass energy of 187.85 eV and individual high-resolution spectra at a pass energy of 23.5 eV with an energy step of 0.1 eV. After taking the surface spectra, depth profiling of the oxidized layers was performed. An Ar^+ ion beam, with an energy level of 3 keV and a raster of 3×3 mm, was used for sputtering. This resulted in a sputtering rate of 1.7 nm/min determined on the Ta_2O_5 standard [27].

The XPS spectra were background-subtracted, using the nonlinear, iterative Shirley method [28]. The fitting procedure allowed signals to be evaluated by determining the peak position, height, width, and Gaussian/Lorentzian ratio [29]. For fixed border conditions, all peak parameters, except height, were kept constant during the deconvolution procedure, i.e., within defined limits.

The spectra recorded for electrochemically oxidized samples were evaluated using parameters of standard peaks (Table 1) [30, 31]. The parameters for metal peaks (Ti and Ni) were recorded on sputter-cleaned samples (no oxide present). An XPS spectrum recorded on Ti thermally oxidized at 450°C for 1 h in an oxygen atmosphere was taken as a standard for TiO_2. Ti suboxides (TiO and Ti_2O_3) were fitted using synthetic spectra obtained as the difference between standard spectra recorded for thermally oxidized samples and those for electrochemically oxidized samples [30]. Ni metal shows the main $2p_{3/2}$ peak at 852.9 eV and a satellite ≈6.5 eV above it, i.e., at 859.4 eV [31]. Ni(II) oxide shows a complex structure, including three peaks in the $2p_{3/2}$ region at 854.6, 856.3, and 861.5 eV [31]. The first two peaks have been attributed to multiplet splitting, whereas the third has been explained by monopole charge transfer processes accompanying ionization of the Ni 2p electrons [32]. The position of the center of the O 1s peak depends on the hydration of the layer and shifts from 532.5 to 530.1 eV as the O^{2-} species increasingly prevails over the OH^- and H_2O species. During deconvolution of spectra, all peak parameters, except height, were kept constant. Border conditions were also kept constant (Table 1).

Table 1 Peak parameters of the standard spectra used for evaluating the anodized NiTi samples

Species	Peak	E_b (eV)	FWHM (eV)
Ti	Ti $2p_{3/2}$	454.2–454.4	1.7–1.8
TiO	Ti $2p_{3/2}$	455.0–455.4	2.3–2.4
Ti_2O_3	Ti $2p_{3/2}$	457.2–457.6	2.3–2.4
TiO_2	Ti $2p_{3/2}$	459.0–459.2	1.3–1.4
Ni	Ni $2p_{3/2}$	852.6–852.9	1.1–1.2
	Ni $2p_{3/2}$ (sat.)	859.4–859.6	2.1–2.2
NiO	Ni $2p_{3/2}$ (m.s.)	854.5–854.8	1.0–1.2
	Ni $2p_{3/2}$ (m.s.)	856.3–856.8	1.2–1.4
	Ni $2p_{3/2}$ (c.t.)	861.5–851.9	2.2–2.4
O^{2-}	O 1s	530.1–530.7	1.6–1.9
OH^-	O 1s	531.2–531.7	1.6–1.9
H_2O	O 1s	532.2–532.7	1.6–1.9

FWHM full width at the half height of peak maximum, *m.s.* multiplet splitting, *c.t.* charge transfer

The following values were used for the calculations: the inelastic mean free electron path: λ(Ti)=1.73 nm, λ(TiO_2)=3.08 nm, λ (Ni)=1.36 nm, λ(NiO)=2.42, and λ (O)=2.97 nm [33]; the Scofield photoionization cross section [34], corrected according to Reilman [35]; Δ(Ti $2p_{3/2}$)=4.70, Δ(Ni $2p_{3/2}$)=13.04, and Δ(O 1 s)=2.51; and the density: ρ(NiTi)=6.5 [36] and ρ(TiO_2)=4.25 gcm^{-3} [37].

Results and discussion

Electrochemical behavior of nitinol in 1 M acetic acid

The general information about the electrochemical behavior of nitinol in 1 M acetic acid was provided by cyclic voltammetry. The cyclic voltammogram presented in Fig. 1 was recorded over a wide potential range, i.e., from hydrogen evolution to oxygen evolution. Two distinct regions were observed, from −0.3 to 0.3 $V_{Ag|AgCl}$, and from 0.4 to 1.2 $V_{Ag|AgCl}$. These regions were ascribed to the formation of a Ti oxide/hydroxide layer containing different titanium oxides [38]. First region corresponds to the formation of titanium suboxides, TiOOH and Ti_2O_3, followed by slight increase in the current density around 0.3 $V_{Ag|AgCl}$ pointing to the transformation of Ti(III) to Ti(IV) oxides. In the second potential region, a near constant anodic current value is observed, indicating thickening of the oxide film with a constant electric field during linear potentiodynamic polarization. This

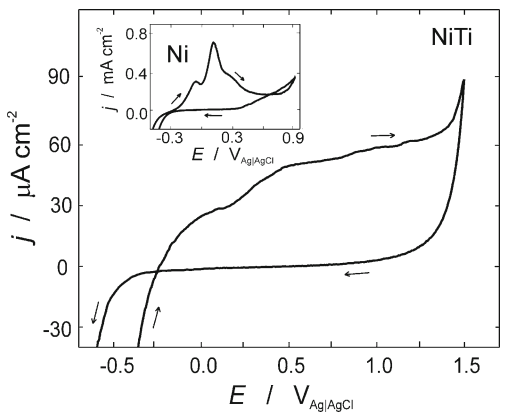

Fig. 1 The cyclic voltammogram of nitinol recorded in 1 M acetic acid with scan rate, ν=10 mV s^{-1}. *Inset*: the cyclic voltammogram of pure nickel recorded under the same conditions

film is constituted mainly of TiO_2 as has been shown by XPS results (see "Characterization of the oxide films on nitinol by X-ray photoelectron spectroscopy" section). Due to the formation of irreducible titanium (IV) oxide, no current peak was observed in the reverse scan. At E=–0.5 $V_{Ag|AgCl}$ hydrogen adsorption and evolution takes place. During the anodic scan, the current increase at $E \geq 1.4$ $V_{Ag|AgCl}$ is related probably to the transpassive nickel dissolution and oxygen evolution [38]. The electrochemical behavior of pure Ni electrodes was investigated under the same conditions (inset in Fig. 1) as for nitinol because of the high content of Ni (50 at.%) in nitinol. The two anodic current peaks are related to the formation of α-$Ni(OH)_2$ and β-$Ni(OH)_2$, and the abrupt increase in the current density at $E>0.8$ $V_{Ag|AgCl}$ is due to nickel dissolution [39]. The shape of the cyclic voltammograms at $E \geq 0.9$ $V_{Ag|AgCl}$ is typical for pitting corrosion.

Kinetics of the oxide film formation and growth

Kinetics of the oxide film formation and growth on nitinol was investigated in 1 M acetic acid (pH=2.7) under galvanostatic and potentiostatic conditions.

Galvanostatic transients (chronopotentiometry) To determine the kinetic parameters of the film growth on nitinol, the galvanostatic transients were recorded in 1 M acetic acid solution at a constant current density ranging from 30 to 100 μA cm^{-2}. Galvanostatic curves presented in Fig. 2a can be divided in three regions: The first region shows an instantaneous rise of potential, the second one presents the oxide film growth at a constant electric field, and the third one shows the potential independence of the time and points to the transpassive nickel dissolution followed by oxygen evolution. In the second potential region, the ionic current, responsible for the oxide growth, is large in comparison with the electronic and the dissolution currents. During the oxide film growth at a constant current density, every newly formed segment of the oxide film demands a potential rise to maintain both the electric field across the film and the anodization current constant. Hence, the rate of potential rise with time in the second region is a measure of the rate of the oxide thickness increase; the slope of the linear part of galvanostatic curve, $(dE/dt)_j$, represents the rate of the oxide formation. The efficiency of the ionic current density consumed for the oxide film formation on NiTi is ≈100% because the value of the empirical constant $b \approx 1$, which was determined using the empirical relation: $(dE/dt)_j = a\ (j)^b$ [40, 41].

The flow of ionic current across the growing oxide film is a field-assisted process. Under the high-field conditions, the relation between the ionic current, j, and the electric field strength, H—the so-called high-field approximation—is valid [40]:

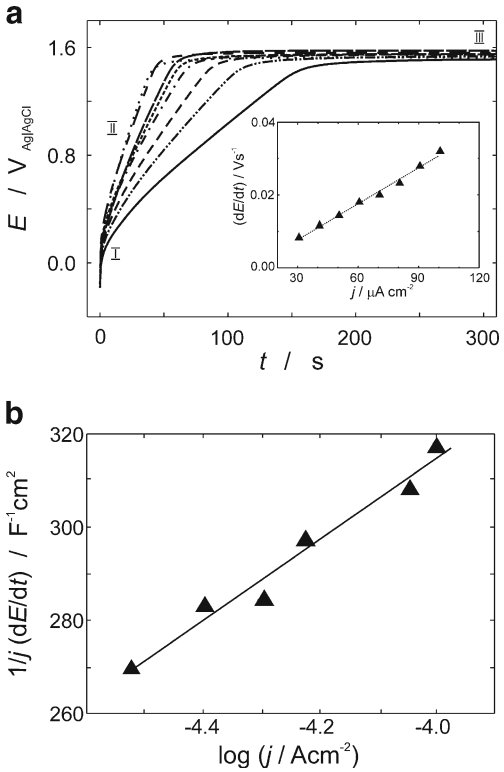

Fig. 2 **a** Galvanostatic transients curves of the nitinol electrode recorded in 1 M acetic acid at different formation current densities, from j=30 μA cm^{-2} (*solid line*) to 100 μA cm^{-2} (*dotted line*). *Inset*: the dependence of the rate of oxide film formation, $(dE/dt)_j$, against the current density, j. **b** The dependence of $1/j(dE/dt)$ against log j

$$j = A\exp(BH) \tag{2}$$

where A and B are kinetic parameters of the oxide film growth. Thus, the rate of the oxide formation, $(dE/dt)_j$ [40], can be expressed using kinetic parameters A and B according to the following equation:

$$\left(\frac{dE}{dt}\right)_j = \frac{2.303rj}{\sigma B}\log\left(\frac{j}{A}\right) \tag{3}$$

The rate of the oxide formation, $(dE/dt)_j$, can also be expressed in the term of electric field strength, H, by substituting the expression $H=(2.303/B)\log(j/A)$, derived from Eq. 2 into Eq. 3

$$\left(\frac{dE}{dt}\right)_j = \frac{rj}{\sigma}H \tag{4}$$

where r is the specific volume of the oxide formed per coulomb, $r=M/(\rho zF)=4.87\times10^{-5}$ cm^3 C^{-1} for TiO_2 (the molar mass of TiO_2, M=79.87 $gmol^{-1}$, the density $\rho(TiO_2)$=4.25 gcm^{-3} [37], the number of electrons interchanged, z=4, and F is the Faraday constant, F=96500 C mol^{-1}). For the surface roughness factor, σ=2 is used, while most of the results obtained on valve metals were calculated

on this basis. The least squares analysis of the of $(dE/dt)_j$ against j set of data, shown in the inset of Fig. 2a, indicates linearity (the correlation coefficient of 0.99). From the slope and using Eq. 4, the electric field strength, $H=11.7\times10^6$ V cm^{-1}, was calculated. Consequently, the growth rate of the oxide film on nitinol is equal to 0.9 nm/V; slightly higher values for the oxide film growth on titanium in acetic acid (1.4–2.8 nm/V) were reported [42].

An important parameter used as the criterion of the applicability of the high-field approximation, Eq. 2, is R_j, usually called unitary formation rate or the reciprocal Faradaic pseudo-capacitance of the film formation, C^{-1}, which is derived from Eq. 3 by dividing both sides by the current density, j [41]. Thus,

$$R_j = \frac{1}{C} = \frac{1}{j}\left(\frac{dE}{dt}\right)_j = \frac{2.303r}{\sigma B}\log\left(\frac{j}{A}\right) \quad (5)$$

Since Eq. 5 is based on the exponential law (Eq. 2), linear relationship between reciprocal capacitance and log j presented in Fig. 2b suggests that the anodic oxide growth on nitinol in acetic acid occurs according to the high-field approximation. Thus, the kinetic parameters of the oxide film growth, A and B, and the ionic conductivity, σAB, can be calculated from the slope and the intercept of the straight line of Fig. 2b:

$$A = 2.4\times10^{-8}\ \text{Acm}^{-2}$$
$$B = 7.1\times10^{-7}\ \text{cmV}^{-1}$$
$$\sigma AB = 3.4\times10^{-14}\ \text{Scm}^{-1}.$$

From the field coefficient B, the half-barrier width (jump distance) of symmetrical barrier for the ionic transport, a^*, was calculated

$$B = \frac{zFa^*}{\Re T} = \frac{qa^*}{k_B T} \quad (6)$$

where q is the charge of the mobile ion, $\Re$ is the universal gas constant, k_B is the Boltzmann constant, and T is the temperature. The half-barrier width (jump distance), $a^*=0.046$ nm, was calculated. The oxide growth parameter, B, and the half-barrier width, a*, are of the same order of magnitude as those previously reported [41].

During in situ galvanostatic oxide film formation, ionic conductivity prevails and both anions and cations move under the influence of high electric field. To discuss transport of charge carriers during in situ anodic oxide formation on nitinol, the metal ion transport number, t_M, was determined using Eq. 1. For calculation, the following values were used: (a) experimentally measured electric field strength, $H=11.7\times10^6$ V cm^{-1}; (b) dielectric constant for amorphous TiO_2, $\varepsilon=40$; (c) the radius of the cluster, $r_0=3.57\times10^{-8}$ cm; (d) dimensionless constant related to overlap cluster before and after vacancy jump, $\gamma=0.2929$, defined by "defect cluster" mechanism [24]. Using values (a)–(d), we obtained $t_M=0.43$. The calculations yield metal transport number that was in good agreement with experimentally determined value for titanium dioxide [18, 20]. Note that according to the model, the metal ion transport number increases with electric field and also depends on the dielectric constant and cluster size.

Potentiostatic transients (chronoamperometry) Potentiostatic transients of nitinol in 1 M acetic acid were recorded at several selected potential values within the passive potential region (see Fig. 1) in order to determine the passive current densities, j_p. As an example, the transient recorded at 0.9 $V_{Ag|AgCl}$ is presented in Fig. 3. The current density of nitinol decreased with passivation time and reached the steady-state value ($j_p=8\times10^{-8}$ A cm^{-2}) after 24 h. A long time period (20–24 h) has been often reported as sufficient to reach the steady-state current density [43]. During this time period, reorganization and "film aging" occurs.

As was mentioned before, in the more crystalline oxide films, the ionic and electronic conductivity are controlled by the transport rate of point defects (metal and oxygen vacancies) [23, 25]. To determine the type of dominant charge carriers, the point defect model (PDM) diagnostic criteria were used [23, 25, 43].

The inset of Fig. 3 shows that the logarithm of passive current density does not depend on the film formation potential, E_f. The PDM states that $\partial \ln j_p/\partial E_f$ for passive film is linearly proportional to $(\delta-\chi)$, where δ is the charge on the cation ejected from the passive film and χ is a stoichiometric parameter for $MO_{\chi/2}$ passive film [23, 25]. In the case of the passive film on NiTi, it is $\delta=\chi=4$, which means $\partial \ln j_p/\partial E_f = 0$ as shown in the inset in Fig. 3. PDM diagnostic criteria postulate independence of the logarithm j_p on E_f, providing that the principal defects are anion (oxygen) vacancies $\left(V_O^{2+}\right)$ [43]. This is consistent with *n*-

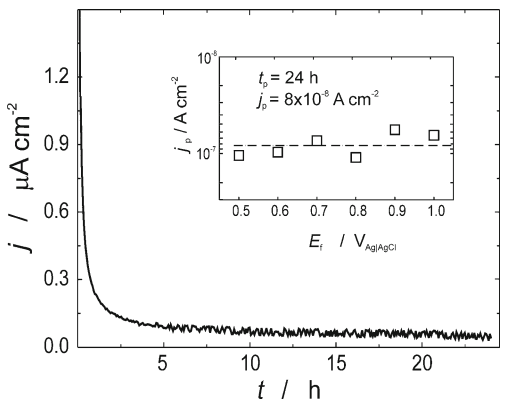

Fig. 3 The potentiostatic transient of nitinol recorded at 0.9 $V_{Ag|AgCl}$ in 1 M acetic acid. *Inset*: the dependence of the passive current density on the film formation potential

type character of the passive film on nitinol, as determined by Mott–Schottky measurements, which will be discussed later (see "Electronic–semiconducting properties of the oxide films on nitinol" section).

Therefore, the key parameter in describing the transport and hence the kinetics of the film growth is the diffusivity of the oxygen vacancies, $D_{Ö}$ [44]. $D_{Ö}$ can be calculated on the basis of the surface charge approach proposed by Bojinov [45] and on Fromhold equation for the high-field strength approximation [17]. In summary, $D_{Ö}$ can be expressed using the following relation, in which all the terms in the right side are either measurable or constant:

$$D_{Ö} = \frac{2a^{*}J_{Ö}}{w_2 \exp\left[zFa^{*}H/(\Re T)\right]} \tag{7}$$

where H, a^{*}, $J_{Ö}$, and w_2 were determined experimentally from galvanostatic, potentiostatic, and capacitance measurements. The steady-state flux of oxygen vacancies, $J_{Ö}$, is defined as $J_{Ö}=-j_p/2e$ and equals to 2.3×10^{11} $s^{-1}cm^{-2}$. The value of the experimental parameter, $w_2=1.91\times10^{19}$ cm^{-3}, was calculated from the donor density, N_D, dependence on E_f (will be discussed in "Electronic–semiconducting properties of the oxide films on nitinol" section).

The substitution of numerical values into Eq. 7 gave the value for $D_{Ö}$ equal to 1.67×10^{-18} cm^2 s^{-1}. Since the process corresponds to solid-state diffusion, the diffusion coefficient is very low. The similar value for diffusivity of oxygen vacancies across the anodic Ti(IV) oxide film was reported for titanium vanadium alloy [38], although the direct comparison of $D_{Ö}$ values in these studies is difficult because of different solutions and materials used.

It must be stressed that a comparison of $D_{Ö}$ is, generally, difficult because the diffusivity of point defects inside the oxide films strongly depends on the experimental conditions, the equations used for calculation, and the film formation time. For example, Bojinov [45] reported that the diffusivity of oxygen vacancies in the passive film formed on W in 1 M H_3PO_4 solution calculated by Eq. 7 is 3 orders of magnitude lower than that obtained by Sikora et al. [46], who performed calculation using low-field approximation. Shorter passivation time results in overestimation of $D_{Ö}$ because the current flow through the passive film under these conditions is much higher than at the steady state [47].

Characterization of the oxide films on nitinol by X-ray photoelectron spectroscopy

XPS spectra were recorded on the oxide films potentiostatically formed on nitinol at selected potentials: E_{OCP} (−0.04 $V_{Ag|AgCl}$), 0.1, 0.75, 0.9, and 1.1 $V_{Ag|AgCl}$ (Fig. 4a–c). Besides the main elements titanium, nickel, and oxygen, contaminants like carbon and a small amount of nitrogen were also detected.

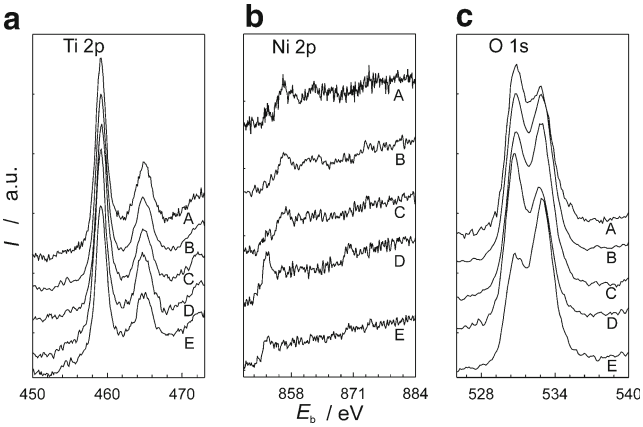

Fig. 4 Normalized **a** Ti 2p, **b** Ni 2p, and **c** O 1s XPS spectra recorded for the oxide films formed potentiostatically on nitinol in 1 M acetic acid at the various potentials: E_{OCP}=−0.04 $V_{Ag|AgCl}$ (*A*), 0.1 $V_{Ag|AgCl}$ (*B*), 0.75 $V_{Ag|AgCl}$ (*C*), 0.9 $V_{Ag|AgCl}$ (*D*), and 1.1 $V_{Ag|AgCl}$ (*E*)

Titanium Regardless of the formation potential, the center of the Ti $2p_{3/2}$ peak appeared in the oxide range, at 459.2 eV (Fig. 4a). The spectra were deconvoluted into four component peaks for Ti, TiO, Ti_2O_3, and TiO_2 (Table 1). For two selected potentials—E_{OCP} (−0.04 $V_{Ag|AgCl}$) and 0.9 $V_{Ag|AgCl}$—the deconvoluted Ti 2p spectra for oxide films formed are presented in Fig. 5a, b as examples of deconvolution procedure. The intensities of individual component peaks in the Ti $2p_{3/2}$ peak expressed as percentage to the total intensity of the Ti $2p_{3/2}$ peak are given in Table 2. The intensity of TiO peak was below 1% and was neglected. Therefore, the spectra were separated into Ti metal, Ti_2O_3 suboxide, and TiO_2 oxide component peaks. As the potential increases, the intensity of metal and Ti_2O_3 decrease (Table 2). The intensity of the TiO_2 peak predominates at all potentials analyzed and increases with increasing potential, i.e., it comprises 70% and 86% of the total peak intensity after polarization at E_{OCP} (−0.04 $V_{Ag|AgCl}$) and 0.9 $V_{Ag|AgCl}$, respectively. Therefore, at lower potentials (−0.04 and 0.1 $V_{Ag|AgCl}$), in the range of the first current plateau (Fig. 1), the content of low-valence oxide Ti_2O_3 is higher and that of TiO_2 is lower than at higher potentials (0.75 V, 0.9 V, and 1.1 $V_{Ag|AgCl}$), i.e., in the range of the second current density plateau at E>0.4 $V_{Ag|AgCl}$ (Fig. 1).

Nickel After oxidation at potentials −0.04 and 0.1 $V_{Ag|AgCl}$, i.e., in the range of first anodic plateau, nickel is present in its metal state, as evident by the position of the peak at 852.6 eV (Fig. 4b). Only after oxidation at higher potentials (0.75 V, 0.9 V, and 1.1 $V_{Ag|AgCl}$), nickel is oxidized and NiO becomes incorporated into the passive film. This is reflected in the shift of the center of the Ni $2p_{3/2}$ peak from 852.6 to 854.5 eV (Fig. 4b). The spectra were deconvoluted into two

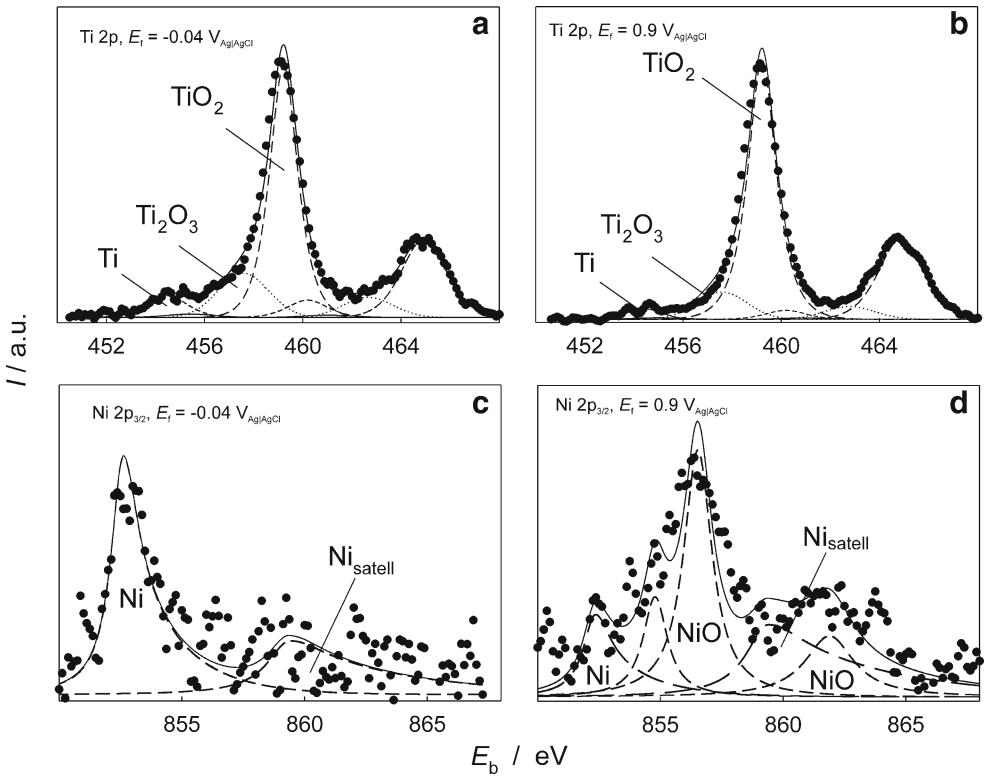

Fig. 5 Deconvoluted **a**, **b** Ti 2p and **c**, **d** Ni 2p XPS spectra recorded for the oxide films formed potentiostatically on nitinol in 1 M acetic acid at E_{OCP}(−0.04 $V_{Ag|AgCl}$) (**a**, **c**) and 0.9 $V_{Ag|AgCl}$ (**b**, **d**)

component peaks, Ni and NiO (Table 1). The deconvoluted Ni $2p_{3/2}$ spectra for oxide films presented for two selected potentials, E_{OCP} (−0.04 V) and 0.9 $V_{Ag|AgCl}$, are given in Fig. 5c, d. The intensities of individual component peaks in the Ni $2p_{3/2}$ peak expressed as percentage to the total intensity of the Ni $2p_{3/2}$ peak are given in Table 2. It is evident from the results given in Table 2 that for anodic potentials lower than 0.75 $V_{Ag|AgCl}$, the nickel signal is comprised of metal part only; polarization at $E \geq 0.75$ $V_{Ag|AgCl}$ results in the formation of nickel oxide, which becomes the predominant nickel species in the film. Its intensity increases with increasing potential (Table 2). The formation of a certain amount of nickel hydroxide cannot be ruled out. Due to the complexity of the Ni $2p_{3/2}$ peak and the low amount of nickel in the film, it is difficult to differentiate between these two species. Like NiO, Ni(II) hydroxide also shows a complex structure, including two peaks in the $2p_{3/2}$ region at 856.6 and 862.4 eV [32].

Table 2 Contribution of particular component peaks, expresses as percentages to the total intensity of the Ti $2p_{3/2}$ peak, Ni $2p_{3/2}$, and O 1s peak, as a function of oxidation potential of nitinol in 1 M acetic acid, as deduced from XPS data (Fig. 4)

E ($V_{Ag\|AgCl}$)	Peak intensity (%)							
	Ti			Ni		O		
	Ti	Ti_2O_3	TiO_2	Ni	NiO	O^{2-}	OH^-	H_2O
−0.04	8.1	21.5	70.4	100.0	0	36.0	3.0	61.0
0.10	5.3	17.3	77.4	100.0	0	41.3	12.4	45.7
0.75	4.2	15.3	80.5	33.0	67.0	40.0	13.3	46.8
0.90	3.7	14.1	82.2	24.0	76.0	32.6	15.1	52.2
1.10	2.0	11.7	86.3	19.0	81.0	33.2	19.1	47.6

Oxygen In the O 1s spectra recorded at E_{OCP} (−0.04 $V_{Ag|AgCl}$), the peak related to the oxide formation (O_{2-} component, Table 1) prevails, while after oxidation at higher potentials the peak related to the hydrated oxygen species (OH^- and H_2O components, Table 1) gradually dominates (Fig. 4c). By deconvolution of the O 1s signal into component peaks of O^{2-}, OH^-, and H_2O, the intensities of individual component peaks are obtained (Table 2). The contribution of hydrated oxygen species (OH^- and H_2O) is significant and depends on applied oxidation potential; inside the potential region 0.1–1.1 $V_{Ag|AgCl}$, it changes from 58.1% to 67.3%. At the same time, the contribution of O^{2-} component ranges from 36.0% to 33.2%. Since the layer was exposed to air before XPS measurements, the exact degree of layer hydration cannot be accounted for.

Based on the XPS results presented in Figs. 4 and 5 and Table 2, it can be concluded that the passive layer formed by potentiostatic oxidation of nitinol in 1 M acetic acid is mainly composed of TiO_2, which is probably hydrated. At $E \geq 0.75$ $V_{Ag|AgCl}$, nickel enters the passive film in the form of NiO. Its content in the layer is very low only 2 and 4 at.% after polarization at 0.75 and 1.1 $V_{Ag|AgCl}$. Expressed as the

ratio between Ti and Ni, the Ti/Ni ratio is 11.5 after polarization at 0.75 $V_{Ag|AgCl}$ and 8.1 at 1.1 $V_{Ag|AgCl}$. Similar ratios of Ti/Ni have been observed by other authors [5, 48–51]. Low nickel content in the oxide layer is important from the biocompatibility point of view because it is well-known that nickel is a common allergen [6], whereas titanium has no known harmful effects. The very low nickel content in the passive layer can be explained by the significantly different values of free energy of formation, for these two oxides [5]. At low oxygen pressure (10^{-4} Torr of oxygen) and at room temperature, Ti is oxidized to TiO_x and TiO_2, while Ni remains in the metallic form, even after 40 min of exposure to oxygen [5]. Preferential oxidation of one of the components has been observed in other systems, e.g., Ti–6Al–4V alloy [30], Ni–Co, Ni–Cr, and Ni–Cr–Fe [5].

The thickness of the oxide layer was calculated according to the model of Hoppe and Strehblow [52]. Potentiostatic polarization induces an increase in film thickness from 8.2 to 8.8 nm after polarization from 0.75 to 1.1 $V_{Ag|AgCl}$, respectively.

Barrier properties of oxide films on nitinol

The barrier (electric and dielectric) properties of the passive oxide films potentiostatically formed on nitinol were investigated by EIS. The impedance spectra recorded on Nitinol covered by the oxide film potentiostatically formed in 1 M acetic acid at the film formation potential ranging from 0.5 to 1.0 $V_{Ag|AgCl}$ are presented in the form of Bode magnitude and phase angle plots in Fig. 6. It is evident that the passivated nitinol electrodes show almost a capacitive behavior within a broad frequency region in which the slope of the log $|Z|$ vs. log f straight lines is close to −1 and the phase angle approaches −90°. At all E_f values, the magnitude of the impedance exceeds 10^6 Ω cm^2 at the frequency of 10 mHz, at which the low-frequency limit is not reached.

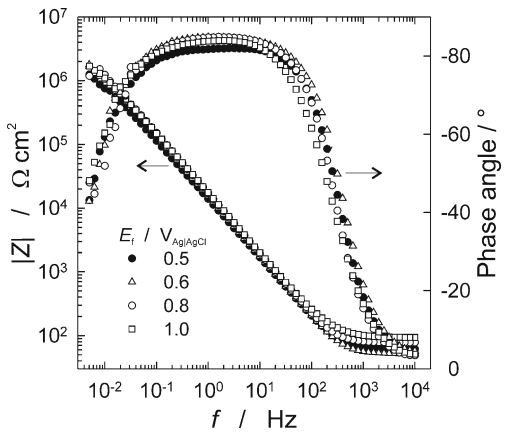

Fig. 6 Impedance spectra of nitinol in 1 M acetic acid recorded after 24 h of potentiostatic film stabilization

The experimental impedance data were fitted using the CNLS algorithm developed by Boukamp [53]. They are analyzed in terms of an R–C parallel combination in series with the electrolyte (ohmic) resistance, R_{el} (Randles equivalent circuit), where C represents the interfacial capacitance at the oxide | electrolyte interface and R is the corresponding polarization resistance. It is noteworthy to mention that the polarization (charge transfer) resistance, R_p, and the oxide film resistance, R_{ox}, are in series and consequently cannot be determined separately. Thus, since $R_p \leq R_{ox}$, it can be assumed that the value of R_{ox} is directly accessible through the fitting procedure. Because the impedance data of a solid | electrolyte interface often reveal a frequency dispersion that is attributed to a "capacitive dispersion," the capacitance is expressed in terms of the constant-phase element (CPE) [54]. Its impedance can be defined as $Z(\mathrm{CPE}) = [Q(j\omega)^n]^{-1}$, where Q is the constant (with dimensions Ω^{-1} cm^{-2} s^n), ω is the angular frequency, and n is the CPE power. When $n=1$, Q has units of a capacitance and represents the interfacial capacitance. When $n \neq 1$, it is generally believed to originate from a distribution in the current density along the electrode surface as result of surface inhomogeneity [55]. Using the frequency independent constant, Q, and the exponent n of the CPE, the interfacial capacitance, C, was calculated using a modified Randles circuit and the expression proposed by Brug et al. [55]:

$$C = Q^{\frac{1}{n}} \left[R_{el}^{-1} + R_p^{-1} \right]^{\frac{n-1}{n}} \tag{8}$$

The value of C is directly related to the oxide layer thickness, d, according to the formula for a parallel plane condenser

$$d = \varepsilon \varepsilon_0 S / C \tag{9}$$

where ε is the dielectric constant of the surface film (ε=61) [56], ε_o is the dielectric constant of vacuum, and S is the electrode surface. The EIS parameters and the film thickness obtained are listed in Table 3. The numerical values of R_p and d allow a rough estimation of the electrical resistivity of the oxide layer to be made, equal to 3×10^{12} Ω cm. The values of the layer thickness deduced from the EIS data are in good agreement with those obtained from XPS measurements (see "Characterization of the oxide films on nitinol by X-ray photoelectron spectroscopy" section).

Electronic–semiconducting properties of the oxide films on nitinol

Electronic properties of the passive oxide films potentiostatically formed on nitinol, under conditions in which their electronic conductivity prevails, were studied in terms of the band-structure model (semiconductor model) [57]. For a

Table 3 Impedance parameters of a nitinol electrode covered by a potentiostatically formed oxide film recorded at different formation potentials in acetic acid

E_f ($V_{Ag\|AgCl}$)	$Q\times10^6$ (Ω^{-1} cm^{-2} s^n)	n_1	$C\times10^6$ (F cm^{-2})	R_p (MΩ cm^2)	d (nm)
0.5	13.47	0.93	7.98	1.86	6.8
0.6	11.27	0.95	7.61	2.24	7.1
0.7	10.51	0.96	7.68	2.59	7.1
0.8	10.14	0.96	7.39	2.10	7.3
0.9	9.51	0.95	6.36	2.89	8.5
1.0	10.45	0.93	5.92	2.87	9.1

semiconductor, the space charge region of the oxide depends on potential and the total capacitance can be written

$$\frac{1}{C_{tot}}=\frac{1}{C_{ox}}+\frac{1}{C_{sc}}+\frac{1}{C_{dl}} \tag{10}$$

where C_{ox} is the capacitance of the oxide film, C_{sc} is the space charge capacitance, and C_{dl} is the double layer capacitance. The double layer capacitance for the oxide water interface is in the order of 100 μF cm^{-2} [58, 59]. Since the capacitances are connected in series, the lowest capacitance will dominate, and therefore, the contribution of C_{dl} to the total capacitance is negligible.

The most common in situ method for probing the electronic properties of the passive films is MS analysis. Figure 7 shows the Mott–Schottky plots for the passive films formed on NiTi for 24 h at various film formation potentials. Thus, the linear dependence of the space charge capacitance, C_{sc}^{-2} against potential, E, with a positive slope is observed suggesting n-type semiconducting behavior, described by the relation [60]:

$$\frac{1}{C_{sc}^2}=\frac{2}{\varepsilon\varepsilon_0 eN_D}\left(E-E_{fb}-\frac{k_BT}{e}\right) \tag{11}$$

where N_D is the donor density, E is the electrode potential, E_{fb} is the flat band potential, e is the electron charge, and the meaning of the other symbols has been given. From the slopes of the MS plots, using Eq. 11, the charge carrier densities were determined. The values of N_D range from 1.2×10^{20} to 0.6×10^{20} cm^{-3} indicating that the oxide layer behaves like a highly doped n-type semiconductor [59]. It was observed that N_D decreased exponentially with E_f in accordance with the theory, and relevant equation describing this dependence is given [46]

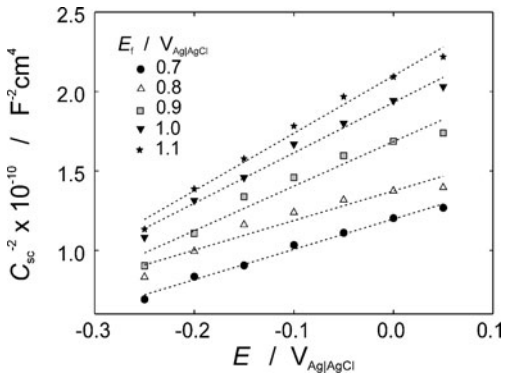

Fig. 7 Mott–Schottky plots of the nitinol electrode covered by the oxide films formed potentiostatically at the various potentials in 1 M acetic acid

$$N_D=w_1\exp[-bE_f]+w_2 \tag{12}$$

where w_1, w_2, and b are unknown parameters that can be determined from the experimental data. Based on the nonlinear fitting of the experimental data, the dependence of N_D on E_f is found to follow the first-order exponential function:

$$N_D=4.70\times10^{20}\ cm^{-3}\exp\left[-2.16\ V^{-1}\times E_f\right]+1.91\times10^{19}\ cm^{-3} \tag{13}$$

The theoretical relationship (Eq. 12) yields a good fit to the experimental results (Eq. 13) and allows the diffusivity of the defects in the passive film to be calculated using the value of parameter, $w_2=1.91\times10^{19}$ cm^{-3} (see "Kinetics of the oxide film formation and growth" section).

Conclusions

The oxide film structure plays significant role in the ionic conductivity mechanism during oxide film formation and growth. The in situ growth of the amorphous oxide films on nitinol under galvanostatic conditions in acetic acid is a high-field-assisted process, which proceeds by a cooperative ion conduction mechanism, which includes both metal and oxygen ions migration. The relevant kinetic parameters for ionic conduction in amorphous oxide films on nitinol were estimated as follows:

- The electric field strength, $H=11.7\times10^6$ V cm^{-1}
- The kinetic parameter of the oxide film growth, $A=2.4\times10^{-8}$ A cm^{-2}
- The field coefficient, $B=7.1\times10^{-7}$ cm V^{-1}
- The ionic conductivity, $\sigma AB=3.4\times10^{-14}$ S cm^{-1}
- The half-barrier width jump distance for the ionic transport, $a^*=0.046$ nm
- The metal ion transport number, $t_M=0.43$

In the passive crystalline film, formed under potentiostatic conditions, which possess a certain rigid lattice or sublattice oxide structure, preponderance of anion vacancies over cation vacancies was established according to the PDM diagnostic criteria. The flux and diffusivity of oxygen vacancies through the film were calculated using experimentally determined kinetics parameters:

- The steady-state flux of oxygen vacancies, $J_{Ö}=2.3\times 10^{11}\ s^{-1}cm^{-2}$
- The diffusion coefficient of oxygen vacancies, $D_{Ö}=1.67\times10^{-18}\ cm^2\ s^{-1}$.

Electronic, semiconducting properties of the passive crystalline films were investigated in the conditions in which electronic conductivity prevails. The *n*-type semiconducting character of the passive films indicates that oxygen vacancies formed during the film formation and growth act as electron donors.

The oxide film formed on nitinol in acetic acid contains mainly TiO_2 with only 2% of Ni. Few nanometers thick passive film on nitinol shows high protecting resistance against chemical degradation (corrosion) of nitinol. These are the key-governing biocompatibility factors determining nitinol implantation possibility.

References

1. Shabalovskaya SA (2002) Bio-Med Mater Eng 12:69–109
2. Firstov GS, Vitchev RG, Kumar H, Blanpain B, Humbeeck JV (2002) Biomaterials 23:4863–4871
3. Morgan NB (2004) Mater Sci Eng A 378:16–23
4. Shabalovskaya SA, Anderegg J, van Humbeeck J (2008) Acta Biomater 4:447–467
5. Chan CM, Trigwell S, Duerig T (1990) Surf Inter Anal 15:349–354
6. Granchi D, Ciapetti G, Savarino L, Stea S, Filippini F, Sudanese A, Rotini R, Giunti A (2000) Biomaterials 21:2059–2065
7. Heintz C, Riepe G, Birken L, Kaiser E, Chakfe N, Morlock M, Delling G, Imig H (2001) J Endovasc Ther 8:248–253
8. Liu X, Chu PK, Ding C (2004) Mater Sci Eng R47:49–121
9. Petrović Ž, Katić J, Metikoš-Huković M, Dadafarin H, Omanovic S (2011) J Electrochem Soc 158:159–165
10. Wever DJ, Veldhuizen AG, de Vriews J, Busscher HJ, Uges DRA, van Horn JR (1998) Biomaterials 19:761–769
11. Cheng FT, Shi P, Pang GKH, Wong MH, Man HC (2007) J Alloys Compd 438:238–242
12. Shi P, Cheng FT, Man HC (2007) Mater Lett 61:2385–2388
13. Chu CL, Wang RM, Hu T, Yin LH, Pu YP, Lin PH, Dong YS, Guo C, Chung CY, Yeung KWK, Chu PK (2009) J Mater Sci: Mater Med 20:223–228
14. Kawakita J, Stratmann M, Hassel AW (2007) J Electrochem Soc 154:C294–298
15. Young L (1961) Anodic oxide films. Academic, London
16. Pringle JPS (1980) Electrochim Acta 25:1423–1437
17. Fromhold AT Jr (1976) In: Diggle JW, Vijh AK (eds) Oxides and oxide films, vol 3. Marcel Dekker, New York, pp 1–271
18. Lohrengel MM (1993) Mater Sci Eng R11:243–294
19. Pringle JPS (1973) J Electrochem Soc 120:398–407
20. Khalil N, Leach JSL (1986) Electrochim Acta 31:1279–1285
21. Pyun SI, Hong MH (1992) Electrochim Acta 37:327–332
22. Chao CY, Lin LF, Macdonald DD (1981) J Electrochem Soc 128:1187–1194
23. Macdonald DD (1992) J Electrochem Soc 139:3434–3449
24. Wang MH, Hebert KR (1999) J Electrochem Soc 146:3741–3749
25. Macdonald DD, Urquidi-Macdonald M (1990) J Electrochem Soc 137:2395–2402
26. Friis EP, Anderson JET, Madsen LL, Bonander N, Moller P, Ulstrup J (1998) Electrochim Acta 43:1114–1122
27. Sanz JM, Hofmann S (1983) Surf Inter Anal 5:210–216
28. Moulder JF, Stickle WF, Sobol PE, Bomben KD (1995) In: Chastain J, King RC Jr (eds) Handbook of X-ray photoelectron spectroscopy. Physical Electronics, Eden Prairie
29. Wolff M (1992) Thesis, Heinrich-Heine Universität, Düsseldorf
30. Milošev I, Metikoš-Huković M, Strehblow HH (2000) Biomaterials 21:2103–2113
31. Milošev I, Strehblow HH (2000) J Biomed Mater Res 52:404–412
32. Kim KS, Winograd N (1974) Surface Sci 43:635–643
33. Seah MP, Dench WA (1979) Surf Inter Anal 1:2–11
34. Scofield JH (1976) J Electr Spectr Relat Phenom 8:129–137
35. Reilman RF, Msezane A, Manson ST (1976) J Electr Spectr Relat Phenom 8:389–394
36. Memry (2011) Bethel, Connecticut. http://www.memry.com/nitinol-iq/nitinol-fundamentals/physical-properties. Accessed 21 Mar 2011
37. Bunshah B, Gupta BK (eds) (1991) Handbook of tribology. McGraw-Hill, New York, p D-42
38. Metikoš-Huković M, Kwokal A, Piljac J (2003) Biomaterials 24:3765–3775
39. Ries LAS, Da Cunha BM, Ferreira MGS, Muller IL (2008) Corr Sci 50:676–686
40. Omanović S, Metikoš-Huković M (1995) Solid State Ionics 78:69–78
41. Ammar IA, Kamal I (1971) Electrochim Acta 16:1539–1553
42. Sul YT, Johansson CB, Jeong Y, Albrektsson T (2001) Med Eng Phys 23:329–346
43. Nicic I, Macdonald DD (2008) J Nucl Mater 379:54–58
44. Vasquez G, Gonzales I (2007) Electrochim Acta 52:6771–6777
45. Bojinov M (1997) Electrochim Acta 42:3489–3498
46. Sikora E, Sikora J, Macdonald DD (1996) Electrochim Acta 41:783–789
47. Ahn SJ, Kwon HS (2005) J Electroanal Chem 579:311–319
48. Figueira N, Silva TM, Carmezim MJ, Fernandes JCS (2009) Electrochim Acta 54:921–926
49. Shabalovskaya SA, Tian H, Anderegg JW, Schryvers DU, Carroll WU, Van Humbeeck J (2009) Biomaterials 30:468–477
50. Milošev I, Kapun B (2011a) Mat Sci Eng C. doi:10:1016/j.msec.2011.11.007
51. Milošev I, Kapun B (2011b) Mat Sci Eng C. doi:10:1016/j.msec.2011.08.022
52. Hoppe HW, Strehblow HH (1990) Surf Inter Anal 16:271–277
53. Boukamp A (1986) Solid State Ionics 20:31–44
54. Jorcin JB, Orazem ME, Pebere N, Tribollet B (2006) Electrochim Acta 51:1473–1479
55. Brug GJ, van der Eeden ALG, Sluyters-Rehbach M, Sluyters JH (1984) J Electroanal Chem 176:275–295
56. Marsh J, Gorse G (1998) Electrochim Acta 43:659–670
57. Dean MH, Stimming U (1987) J Electroanal Chem 228:135–151
58. Gunnarsson M, Abbas Z, Ahlberg E, Gobom S, Nordholm S (2002) J Colloid Interface Sci 249:52–61
59. Petersson IU, Löberg JEL, Fredriksson AS, Ahlberg EK (2009) Biomaterials 30:4471–4479
60. Morrison SR (1980) Electrochemistry at semiconductor and oxidized metal electrodes. Plenum, New York, p 133